Sensors & Actuators: B. Chemical 418 (2024) 136219

Contents lists available at ScienceDirect

Sensors and Actuators: B. Chemical

journal homepage: www.elsevier.com/locate/snb

Bismuth-MXene nanocomposite: A low-cost portable solution for zinc (II) detection in water for safer environmental monitoring

Sima Singh [a], Ada Raucci [a], Wanda Cimmino [a], Arshid Numan [b,c,*,1], Mohammad Khalid [d,e,f], Stefano Cinti [a,g,h,**,2]

[a] Department of Pharmacy, University of Naples Federico II, Via D. Montesano 49, Naples 80131, Italy
[b] Sunway Centre for Electrochemical Energy and Sustainable Technology (SCEEST), School of Engineering and Technology, Sunway University, No. 5, Jalan Universiti, Bandar Sunway, 47500 Selangor Darul Ehsan, Malaysia
[c] Department of Applied Physics, Saveetha School of Engineering, Saveetha University (SIMATS), Chennai, India
[d] Materials and Metallurgy Research Group, James Watt School of Engineering, University of Glasgow, Glasgow G12 8QQ, UK
[e] Manipal Institute of Technology, Manipal Academy of Higher Education, Manipal 576104, Karnataka, India
[f] University Centre for Research and Development, Chandigarh University, Mohali, Punjab, 140413, India
[g] BAT Center, Interuniversity Center for Studies on Bioinspired Agro-Environmental Technology, University of Napoli Federico II, Naples 80055, Italy
[h] Bioelectronics Task Force at University of Naples Federico II, Via Cinthia 21, Naples 80126, Italy

ARTICLE INFO

Keywords:
Heavy metals
Zinc (II)
Bi_2S_3 -MXene nanocomposite
Electrochemical
Portable

ABSTRACT

The development of a portable and cost-effective sensor for detecting zinc ions (Zn (II)) in water addresses a crucial need for real-time monitoring of heavy metal environmental contamination. To this, here, a novel bismuth-MXene (Bi_2S_3-MXene) nanocomposite-based sensor is developed for the rapid and selective detection of Zn (II) ions with a simple procedure. The exceptionally selective nanocomposites were capable of detecting Zn (II) through the square-wave anodic stripping voltammetry (SWASV) technique in a linearity range of up to 3 μg/mL, achieving limit of detection (LOD) of 7 ng/mL and limit of quantification (LOQ) of 22 ng/mL with a correlation coefficient of R^2 =0.9825. Subsequently, the content of Zn (II) in real tap water and sea water was successfully determined for sensitivity and practical applicability. The developed sensor demonstrated several advantages for detecting Zn (II) in water, including a rapid setup process, fast detection times, high sensitivity, more selectivity and portability. While this study focuses on Zn (II) detection, the developed platform suggests it could potentially be adapted for detecting other heavy metals in future research. This work broadens the potential applications of portable nanomaterial-based sensors for regular environmental monitoring.

1. Introduction

Water is crucial, for the survival of humanity and its significance cannot be overstated [1]. It has the potential to harbor contaminants, including metals like lead (Pb), arsenic (As), zinc (Zn), cobalt (Co), cadmium (Cd), copper (Cu), mercury (Hg), and nickel (Ni). The presence of these contaminants mostly depends on the sources of pollution [2]. Human actions, like transportation, industrialization, farming and mining contribute to the buildup of metal ions, on the Earths surface [3,4]. The pollution has negative effects [5]. The uncontrolled discharge of pollutants, chemicals and improper disposal of waste leads to the introduction of substances, into water sources. According to the UN, toxic metals released into the environment by humans, threaten clean drinking water, contaminate water within the EU region, accumulate in ecosystems [6,7].

Monitoring metals is vital for health as they can dissolve in water, persist, and accumulate in organisms, leading to cancer and other health issues. Ensuring water quality is crucial to protect well-being [8]. Among the different metals, zinc despite its presence, in the body can pose a concern if not properly regulated. Zinc plays an important role for

---

* Corresponding author at: Sunway Centre for Electrochemical Energy and Sustainable Technology (SCEEST), School of Engineering and Technology, Sunway University, No. 5, Jalan Universiti, Bandar Sunway, 47500 Selangor Darul Ehsan, Malaysia.

** Corresponding author at: Department of Pharmacy, University of Naples Federico II, Via D. Montesano 49, Naples 80131, Italy.

E-mail addresses: numan.arshed@yahoo.com (A. Numan), stefano.cinti@unina.it (S. Cinti).

[1] ORCID: 0000–0003-1690–2001

[2] ORCID: 0000–0002-8274–7452

https://doi.org/10.1016/j.snb.2024.136219
Received 26 March 2024; Received in revised form 18 June 2024; Accepted 29 June 2024

enzymes transcription factors and synaptic vesicles in nerve endings that transmit stimulating signals. Moreover, it is involved in regulating the transmission of signals, between neurons and impacting cell survival [9]. Given this dual nature of being both essential and potentially harmful impact, the urgency of accurate and sensitive detection methods for Zn (II) becomes evident.

Currently, the detection of Zn (II) is primarily carried out by using different methods such as inductively coupled plasma optical emission spectrometry (ICP-OES) [10], atomic absorption spectroscopy (AAS) [11], fluorescence [12,13] and energy X-ray spectroscopy (EDS) [14]. Although these techniques are important in laboratory and clinical settings for their sensitivity and accuracy, still there remains a need for more convenient, selective, and real-time information provided by cost-effective detection methods due to the technical complexity associated with current detection technique [15,16]. In contrast, the use of electrochemical detection sensors has become more popular as an eco-friendly solution for applications [16–18]. These sensors combine accuracy, sensitivity, and sustainability, addressing the challenges of heavy metal detection.

On the other hand, nanomaterial-based sensors show promise, in detecting metals due, to their high surface area and excellent adsorption abilities. These qualities enhance the precision and sensitivity of sensors, aligning well with our goal for an environmentally friendly and technologically advanced future [19,20]. Despite the high regulatory limit of zinc set by regulatory authorities like WHO, FDA, US FDA, and EPA, the need for ultrasensitive detection of Zn (II) remains significant, particularly in specific contexts such as biological and environmental studies. As compared to the other metal ions, zinc is reported to be reasonably safe, still poses health risks when accumulated in high concentrations over time. Besides this acute intoxication, long-term use of zinc supplements can interfere with the uptake of copper [21].

Researchers have enhanced detection of Zn (II) using electrochemical methods, achieving high precision and sensitivity. For instance, Qin et al. utilized a modified glassy carbon electrode (GCE) with Hg/CMWCNTs@ZIF-8 to simultaneously detect zinc and copper in fruit juice. The ZIF-8-based sensor demonstrated excellent reliability and specificity, with detection limits of 5.23×10^{-3} and 6.52×10^{-3} mg L^{-1}, respectively [22]. Likewise, Akhtar et al. reported an ultra-sensitive sensor using MXene/Fe_3O_4/g-C_3N_4 for detecting Zn (II), Pb (II), Cd (II), Hg (II), and Cu (II) in tap water, with low detection limits and high selectivity [23].

To this, nanostructures metal oxides (MOs) play an important role in sensing applications with benefits of simple synthesis route, versatile structure, cost-effectiveness and stability [24,25]. Bismuth sulfide (Bi_2S_3) and its nanoparticles are becoming increasingly crucial in electrochemistry due to their n-type semiconductor properties and direct bandgap (around 1.3 eV). This eco-friendly materials are highly effective for biosensors due to their melting point and strong affinity for heavy metal ions, making them suitable for diverse applications in various electrode-related areas [26–28]. The electrical properties of nanoparticles change based on their shape, prompting scientists to prefer two-dimensional materials (2DMs). These 2D materials offer electron mobility are easy to use and're ideal, for developing sensors that produce electrical signals [8]. MXenes, a category of 2D materials [29,30], offer a solution, with mechanical characteristics, excellent electron mobility and easy processing capabilities due, to their extensive surface areas [31]. Moreover MXenes demonstrate excellent conductivity [32].

To address this requirement the mixture integrates Bi_2S_3 and MXene nanoparticles leveraging the advantages of each material. Bi_2S_3 offers semiconducting properties and a strong affinity for metal ions, while MXenes add strength, efficient electron transport, and excellent electrical conductivity. The synergy between these two materials enhances the performance and sensitivity of sensor. In our research, we have developed an electrochemical sensor using a Bi_2S_3-MXene nanocomposite. This sensor effectively detects Zn (II), as shown in Scheme 1.

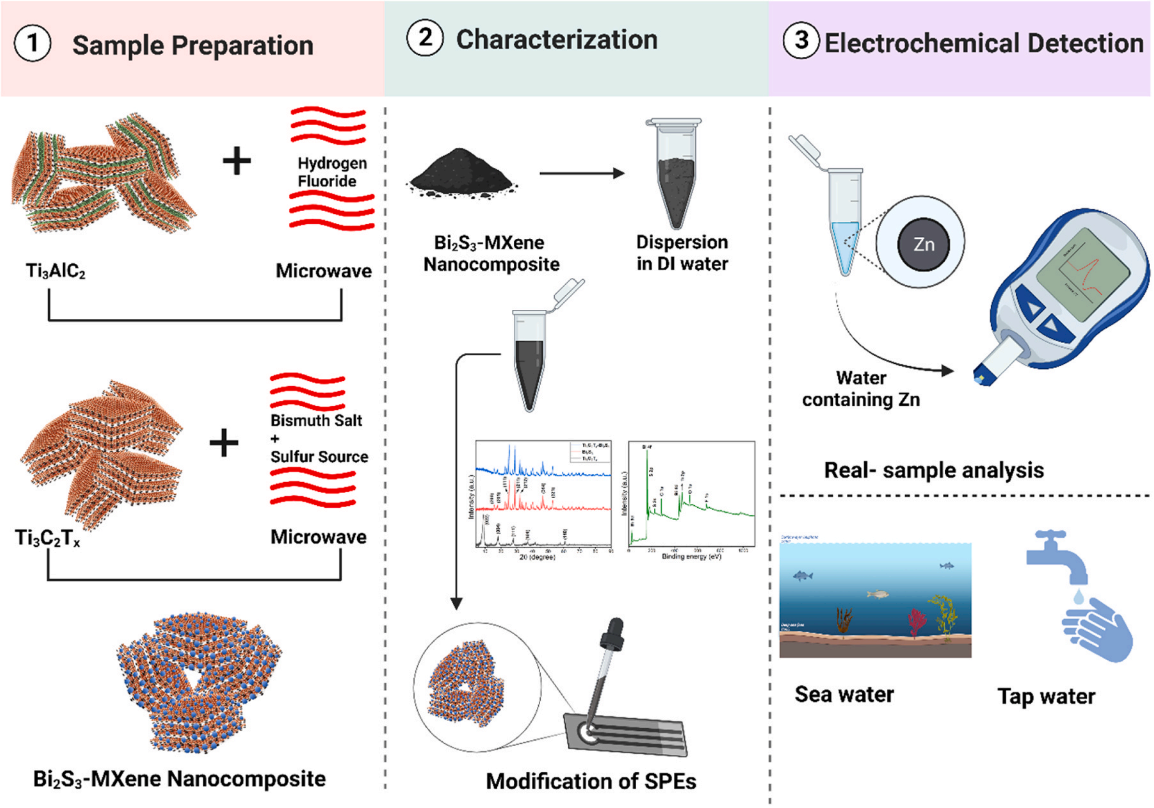

Scheme 1. The schematic illustration depicts the sequence of steps involved in preparation, characterization, and further, making it a versatile tool for environmental monitoring of Zn (II) for electrochemical detection.

By designing the nanocomposite to meet sensing requirements, we have improved the reliability and customization potential of the sensor. These advancements broaden its applications. The development of electrochemical sensors has been a remarkable achievement, and this study provides a comprehensive exploration of their underlying mechanisms.

2. Experimental section

2.1. Chemicals and apparatus

We obtained inks (Ag/AgCl and carbon) from Acheson (Italy). The chemicals used, include potassium ferricyanide ($K_3Fe(CN)_6$), sodium acetate, sodium chloride, hydrochloric acid, zinc solution (1000 μg/L), mercury, copper, iron, lead, silver, cadmium, and magnesium were purchased from Sigma Aldrich (Italy). All the working solutions were prepared using distilled water (DI) from Millipore. The chemicals used in this study were of analytical quality and did not require further processing or changes. To conduct the voltammetric analysis, we utilized a PalmSens 4 potentiostat, The Netherlands. All the electrochemical experiments were carried out at room temperature.

2.2. Sensing principle

The Bi_2S_3-MXene nanocomposite shows promising potential in sensing applications as a material. Square-wave anodic stripping voltammetry (SWASV) is a widely used electrochemical method for detecting metal ions like Zn (II). Bi_2S_3 is used as an electrocatalyst because it has properties, for electron transfer and can effectively catalyze a range of reactions [33]. In contrast, MXenes offer a large surface area [34]. They are also highly conductive, facilitating rapid charge transfer [35]. The use of Bi_2S_3 as the electrocatalyst, along with MXenes as the supporting material, combines their respective advantages. The combination of the surface area and conductivity of MXenes enhances the functionalities of Bi_2S_3, which could lead to electrocatalytic performance through enhanced efficiency. Therefore we used this attribute as the basis, for developing the proposed biosensor. Detecting Zn(II) using SWASV, relies on the adsorption, deposition and removal of metal ions, at the electrodes surface. Within this structure MXene comprises elements, like hydroxyl and oxygen that create a surface, for chemical interactions. This enables the movement of Zn^{2+} ions during processes [36,37]. Bi_2S_3 enhances the sensing process by forming a fused alloy with Zn(II) ions [38].

The sensing mechanism can be represented by the following equations:

Adsorption step:

$Zn^{2+} + 2e^- \rightarrow Zn(s)$ (adsorption)

Stripping step:

During the stripping process, an electrode is subjected to a square wave potential. This reduces the Zn^{2+} ions, which are then oxidized back to Zn^{2+}.

$Zn(s) \rightarrow Zn^{2+} + 2e^-$ (stripping)

The SWASV system's exceptional sensitivity, in conjunction with the characteristics of Bi_2S_3 -MXene nanocomposites, makes it an effective technique for detecting Zn (II) in water.

2.3. Manufacturing of polyester-based printed strips

Screen printing was used to develop screen printed electrodes (SPEs) on a polyester substrate. The fabrication process consisted of two steps, carried out at a temperature. Initially, we employed silver ink (Ag/AgCl) (Electrodag 477 SS) to print the reference electrode. The electrode was dried in an oven at 80 °C for 40 minutes. After that, the working and counter electrodes were printed using carbon ink (Elettrodag 421) and dried in an oven at 80 °C for 40 minutes. The working electrode had a diameter of 0.4 cm, which resulted in an area of 0.07 cm^2. Before conducting experiments, we used tape to mark the contact area and ensure electrical isolation.

2.4. Etching of MXene

To extract $Ti_3C_2T_x$ from its Ti_3AlC_2 MAX phase, we employed a microwave-assisted hydrothermal technique [39]. The Al layer of the MAX phase was etched using HF. Briefly, a 1 g of Ti_3AlC_2 was slowly added to a 20 mL of HF (48–52 %) under constant stirring continuously for 10 minutes. The mixture was transferred to a Teflon high-pressure reactor. The mixture was then heated in a microwave hydrothermal reactor at a rate of 1.5 °C/minute, maintaining a temperature of 80 °C for 30 minutes. After rinsing with DI and ethanol to achieve a pH below 5.0 the solution was centrifuged at a speed of 3000 rpm for five minutes. The resulting Ti_3C_2-MXene was then freeze-dried and stored in an amber-coloured bottle at 4 °C.

2.5. Synthesis of Bi_2S_3

A 1 mmole of Bi_2S_3 nitrate pentahydrate ($Bi(NO_3)_3{\cdot}5\,H_2O$) was dissolve in 60 mL of DI water. A 5 mmole (C_2H_5NS) thioacetamide was slowly added to the above solution under constant stirring. The solution was kept under constant stirring for another 30 minutes and then transferred to a Teflon tube for microwave synthesis at 180 ° C for 10 minutes with a heating rate of 4 ° C per minute. After the reaction the precipitate were collected through centrifugation and it was washed 3 times with DI water. Further, it was kept for freeze drying.

2.6. Synthesis of Bi_2S_3-MXene nanocomposites

In order to prepare Bi_2S_3-Mxene nanocompostes, a 1 mmole of $Bi(NO_3)_3{\cdot}5\,H_2O$ was dissolved in 50 mL of DI water followed by addition of 5 mmole of C_2H_5NS under constant stirring. A 10 mL of (1 mg/mL) of MXene dispersion was added dropwise in the above solution under bath sonication. The mixture was subjected to bath sonication for 30 minutes with purging of N_2 at room temperature. Subsequently, the mixture was transferred to a Teflon tube for microwave synthesis at 180 °C for 10 minutes with a heating rate of 4 ℃ per minute. The precipitates were collected and washed with DI water and ethanol using centrifugation, followed by freeze drying.

2.7. Characterization

The morphological characteristics of the distinctive specimens, including Bi_2S_3, MXene, and the Bi_2S_3-MXene nanocomposite, were examined using a JEOL scanning electron microscope (SEM) instrument. X-ray diffraction (XRD) data were obtained using a PANalytical X′Pert3 powder diffractometer with Cu-Kα radiation ($\lambda = 0.15406$ nm) at 40 kV and 30 mA, covering the 2θ range from 5 to 80 degrees. Fourier-transform infrared spectroscopy (FTIR) analysis used the PerkinElmer Spectrum IR Version. The surface properties of the Bi_2S_3-MXene nanocomposite were investigated using the Thermo Scientific K-Alpha X-ray photoelectron spectroscopy (XPS) instrument. The chamber pressure was maintained below 5×10^{-9} mbar throughout the procedure. High-resolution scans and an overview were obtained using the spectrometer in large-area XL magnetic lens mode, with pass energies set at 150 and 20 eV. Spectra were generated with an electron take-off angle of 90° relative to the surface plane. High-resolution peaks were produced using peak-fitting algorithms from the Advantage software packages (ThermoVG). The binding energies were calculated with reference to the internal C1s peak at 284.9 eV.

2.8. *Preparation of Bi_2S_3-MXene nanocomposites dispersion*

A 1 mg/mL stock solution of Bi_2S_3-MXene nanocomposites was prepared by dispersing in DI water. This stock solution served as the base for the electrode modification process. For modification of electrode, 8 μL of the Bi_2S_3-MXene nanocomposites dispersion was carefully pipetted onto the surface of SPEs. Prior to the application of the nanocomposite dispersion, adhesive tape was fixed to the SPEs to define the area for modification and prevent overflow. Once the dispersion was applied, the electrodes were placed in an oven set at an appropriate temperature to facilitate the drying process. This step ensured that the Bi_2S_3-MXene nanocomposites formed a stable, uniform layer on the SPE surface, ready for subsequent electrochemical experiments.

3. Results and discussion

3.1. *Morphology*

Bi_2S_3-MXene nanocomposites were synthesized using a straightforward microwave-assisted hydrothermal method. The SEM image presented in Fig. 1**A** illustrates the agglomeration of Bi_2S_3 nanoparticles. These nanoparticles exhibit a granular shape with diameters ranging from 70 to 100 nm.

The agglomeration is likely due to van der Waal forces between the nanoparticles [40]. The image shows the agglomeration as the bright clusters of particles. Nanoparticle agglomeration can significantly impact electrochemical performance by reducing the active surface area, hindering mass transport, altering analyte accessibility, and modifying charge transfer dynamics [41,42]. In Fig. 1**B**, shows the SEM image of MXene, demonstrating stacked lamellar structure of MXene after removal of Al layers from MAX phase. These stacked MXene sheets offer high surface area for the target analyte while the voids among MXene sheets can facilitate the intercalation of target molecule to access the inner surface are of MXenes Moreover, higher conductivity of MXene leads to rapid charge transfer kinetics during a redox event [43,44]. The SEM image of Bi_2S_3-MXene nanocomposites is shown in Fig. 1**C and** 1**D** (low and high magnification). It is evident from SEM images that Bi_2S_3 nanoparticles decorated onto the surface of MXene flakes during microwave hydrothermal reaction. The uniform growth of Bi_2S_3 nanoparticles on MXene sheets was due to highly electronegative functional group moieties (F, and OH) which served as anchoring sites for the growth of Bi_2S_3 nanoparticles. Additionally, there is a significant increase in the voids of stacked MXene sheets that might be due to the effect of microwave irradiations open up the gaps between MXene sheets. The synergistic effect of Bi_2S_3 and MXene nanoparticles can enhance the electrochemical performance. Firstly, the MXene provides a highly conductive platform for the uniform growth of Bi_2S_3 nanoparticles. This, leads to the reduction in Bi_2S_3 nanoparticles agglomeration and higher exposure of detection sites for the target analyte [45]. Secondly the MXene exhibits high conductivity, leading to enhanced charge transfer, between the Bi_2S_3 nanoparticles and the electrolyte [46]. Furthermore the property of oxidation resistance exhibited by MXene plays a role, in safeguarding the Bi_2S_3 nanoparticles, against corrosion [47]. The combination of MXene and Bi_2S_3 nanoparticles can result in enhanced performance when detecting Zn (II).

3.2. *Structural analysis of Bi_2S_3-MXene nanocomposite materials*

The XRD patterns for $Ti_3C_2T_X$ (black), Bi_2S_3 (red line), and $Ti_3C_2T_X$ -Bi_2S_3 nanocomposite (blue line) are revealed in Fig. 2**A**.

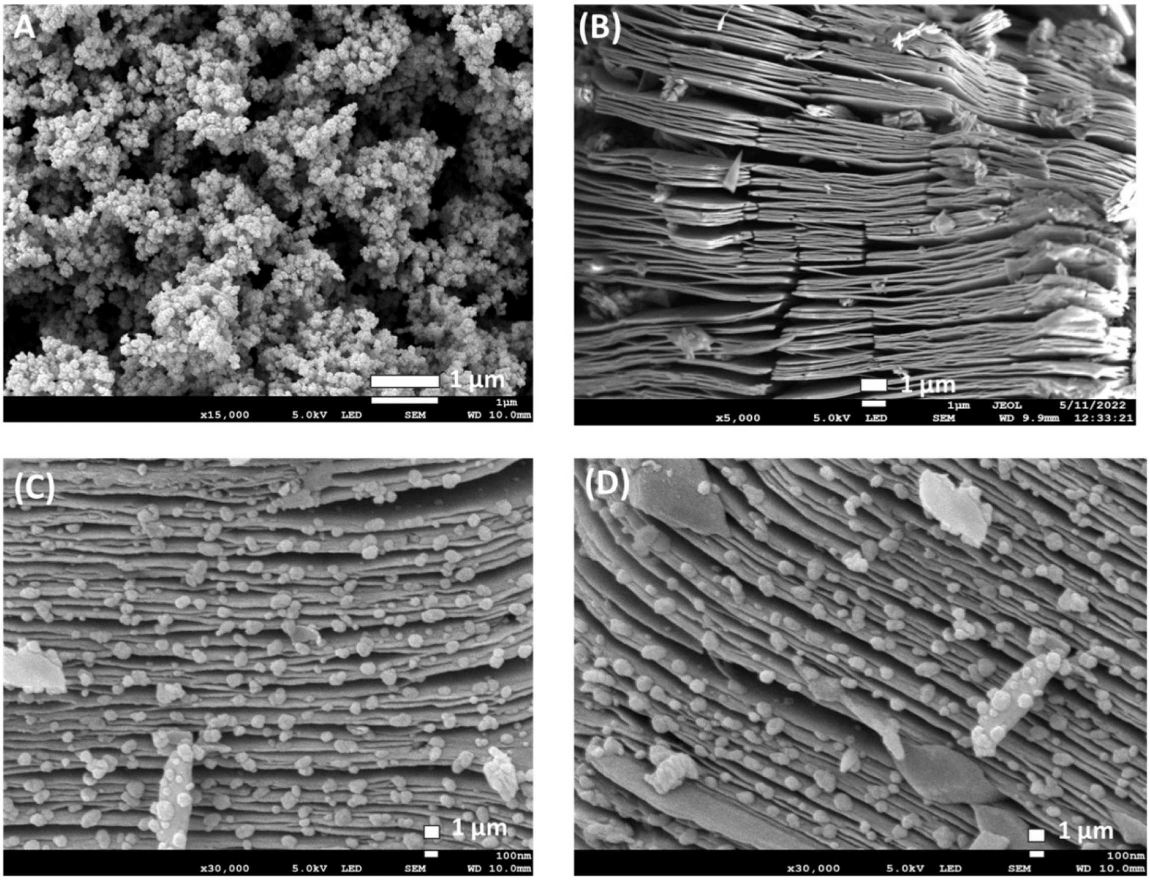

Fig. 1. Structural characterizations of **(A)** Bi_2S_3; **(B)** MXene; **(C)** Bi_2S_3-MXene nanocomposite@ low magnification; **(D)** Bi_2S_3-MXene nanocomposite@ high magnification.

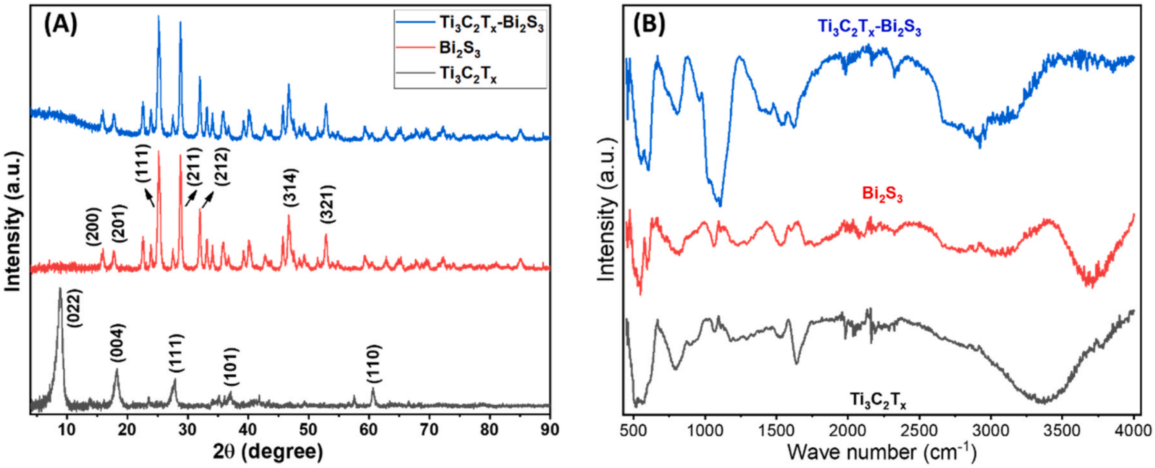

Fig. 2. (A & B) Experimental XRD patterns and FTIR of $Ti_3C_2T_X$ (black), Bi_2S_3 (red line), and Bi_2S_3-Ti_3C_2Tx nanocomposite (blue line).

It shows that the nanocomposite has a hybrid structure that contains both Ti_3C_2Tx and Bi_2S_3 phases. The Ti_3C_2Tx phase is evident from the diffraction peaks at 9° and 61°, which correspond to the (002) and (110) planes of Ti_3C_2Tx, respectively [48]. The Bi_2S_3 phase is evident from the diffraction peaks at 16°, 26°, 32°, and 52°, which correspond to the (111), (200), (221), and (310) planes of Bi_2S_3, respectively [49]. The XRD pattern of the nanocomposite reveals successful integration of Bi_2S_3 into $Ti_3C_2T_X$ MXene sheets. This is crucial for applications because it guarantees interaction between the two materials and maximizes the surface area of the nanocomposite. To achieve the desired effects in electrochemical detection, it is crucial to consider the following: The diffraction peaks of the Bi_2S_3-Ti_3C_2Tx nanocomposite exhibit slight shifts when compared to those of the individual Ti_3C_2Tx and Bi_2S_3 materials. There seems to be some interaction between the two materials in the nanocomposite. The diffraction patterns of the Bi_2S_3-Ti_3C_2Tx nanocomposite seem to show a representation compared to those seen in the Ti_3C_2Tx and Bi_2S_3 materials. The smaller crystal size of the Bi_2S_3-Ti_3C_2Tx nanocomposite suggests that it differs from materials. The fusion of its framework and robust crystallinity suggests that it possesses potential as a substance for numerous electrochemical uses.

Fig. 2B, shows the FTIR spectrum of $Ti_3C_2T_X$ (black), Bi_2S_3 (red line), and Bi_2S_3-Ti_3C_2Tx nanocomposite (blue line). The peak at 572 cm^{-1} is assigned to the TiO bonding in $Ti_3C_2T_X$ (black). The peak at 1019 cm^{-1} is assigned to the C-O stretching vibration, which is likely due to the presence of surface hydroxyl groups on the $Ti_3C_2T_X$ flakes. The peak at 1638 cm^{-1} is assigned to the O-H bending vibration, which is likely due to the presence of surface hydroxyl groups on the $Ti_3C_2T_X$ flakes. The peak at 3456 cm^{-1} is assigned to the O-H and N-H stretching vibration, which is likely due to the presence of surface hydroxyl groups and adsorbed water on the $Ti_3C_2T_X$ flakes. The FTIR spectrum of $Ti_3C_2T_X$ (black) in the image is consistent with the reported FTIR spectra of $Ti_3C_2T_X$ in the literature [50,51]. The presence of the peaks at 672 cm^{-1}, 1019 cm^{-1}, 1123 cm^{-1}, 1638 cm^{-1}, and 3456 cm^{-1} confirms the presence of TiO bonding, C-O bonding, C-F bonding, O-H bending vibration, and O-H and N-H stretching vibration, respectively. These peaks are characteristic of $Ti_3C_2T_X$ [50,51]. The FTIR spectrum of the Bi_2S_3 (red line) nanoparticle sample show distinct peaks that align with the vibrational patterns of the Bi-S bond.

The presence of the Bi-S rocking mode peaks at 547.94 cm^{-1} and 610 cm^{-1} confirms the formation of Bi_2S_3. The interaction between sulfur-atmospheric carbon and oxygen bonding peak at 1300–1370 cm^{-1} is likely due to the presence of surface impurities, such as adsorbed oxygen or carbon dioxide [52]. The O-H bending vibration peaks at 1532.20 cm^{-1} and 1638.04 cm^{-1}, and the N-H stretching vibration peaks at 3064.7 cm^{-1} and 3375 cm^{-1} are likely due to the presence of adsorbed water and/or surface hydroxyl groups. The O-H stretching vibration peak at 3430 cm^{-1} peak suggests that there is some surface oxidation of the Bi_2S_3 powder. This peak suggests that there is some surface oxidation of the Bi_2S_3 powder. The FTIR spectrum of the Bi_2S_3 nanoparticles in the image is consistent with the formation of Bi_2S_3 nanoparticles with some surface oxidation and adsorbed water. Surface oxidation and adsorbed water can have a significant impact on the properties of Bi_2S_3 nanoparticles. It is generally desirable to minimize surface oxidation and adsorbed water on Bi_2S_3 nanoparticles.

The presence of the peaks at 554 cm^{-1}, 610 cm^{-1}, and 1300–1370 cm^{-1} confirms the presence of Bi_2S_3 in the $Ti_3C_2T_X$ -Bi_2S_3 nanocomposite. The presence of the peaks at 672 cm^{-1}, 1019 cm^{-1}, and 1123 cm^{-1} confirms the presence of $Ti_3C_2T_X$ in the $Ti_3C_2T_X$ -Bi_2S_3 nanocomposite. The presence of the peaks at 1638 cm^{-1} and 3375 cm^{-1} suggests that there is some surface oxidation and adsorbed water on the $Ti_3C_2T_X$ -Bi_2S_3 nanocomposite. Overall, the FTIR spectrum of Bi_2S_3-Ti_3C_2Tx in the image is consistent with the formation of a Bi_2S_3-Ti_3C_2Tx nanocomposite with some surface oxidation and adsorbed water.

3.3. X-ray photoelectron spectroscopy

In Fig. 3, we can observe the chemical bonding on the surface of the Bi_2S_3-MXene nanocomposite. This analysis helps us understand the structure of the components and their valence states. To ensure curve resolution, we matched the high-resolution XPS deconvolution spectra at the core level with respect to their background. In Fig. 3**A,** we can see the chemical bonding occurring on the surface of the Bi_2S_3-MXene nanocomposite.

This analysis assists us in embracing the structure of the components and their valence states. To ensure curve resolution, we compared the high-resolution XPS spectra at the core level to their background [53]. These peak binding energies closely align with metallic Bi_2S_3. Furthermore, the presence of Ti 2p and O 1 s peaks serves as compelling evidence for the existence of MXene in the nanocomposite, as their binding energies are consistent with those of titanium and oxygen in MXene [54]. Moreover, the strong presence of S 2p and S 2 s peaks indicates that there are probably sulfur-containing groups on the surface of the nanocomposite. The XPS spectrum of the Ti $2p_{1/2}$ peak shows a single peak at 458.7 eV, indicating Ti^{4+} in TiO_2 (Fig. 3**B)** [55]. The sharpness of this peak suggests a well-defined chemical environment. The Ti $2p_{1/2}$ peak at 458.7 eV hints at an oxygen-terminated TiO_2 surface, in line with expectations. Two peaks are observed in the binding energy values at 163.7 and 158.4 eV. This binding energy is consistent with the Bi 4f7/2 peak of metallic Bi_2S_3 (Fig. 3**C).** Our results are in agreement with the available literature, there isn't a change in the binding energy of the peaks, which suggests that Bi_2S_3 is present in its +3 oxidation state [56]. The XPS spectrum of the oxygen 1 s, in the image you provided, shows

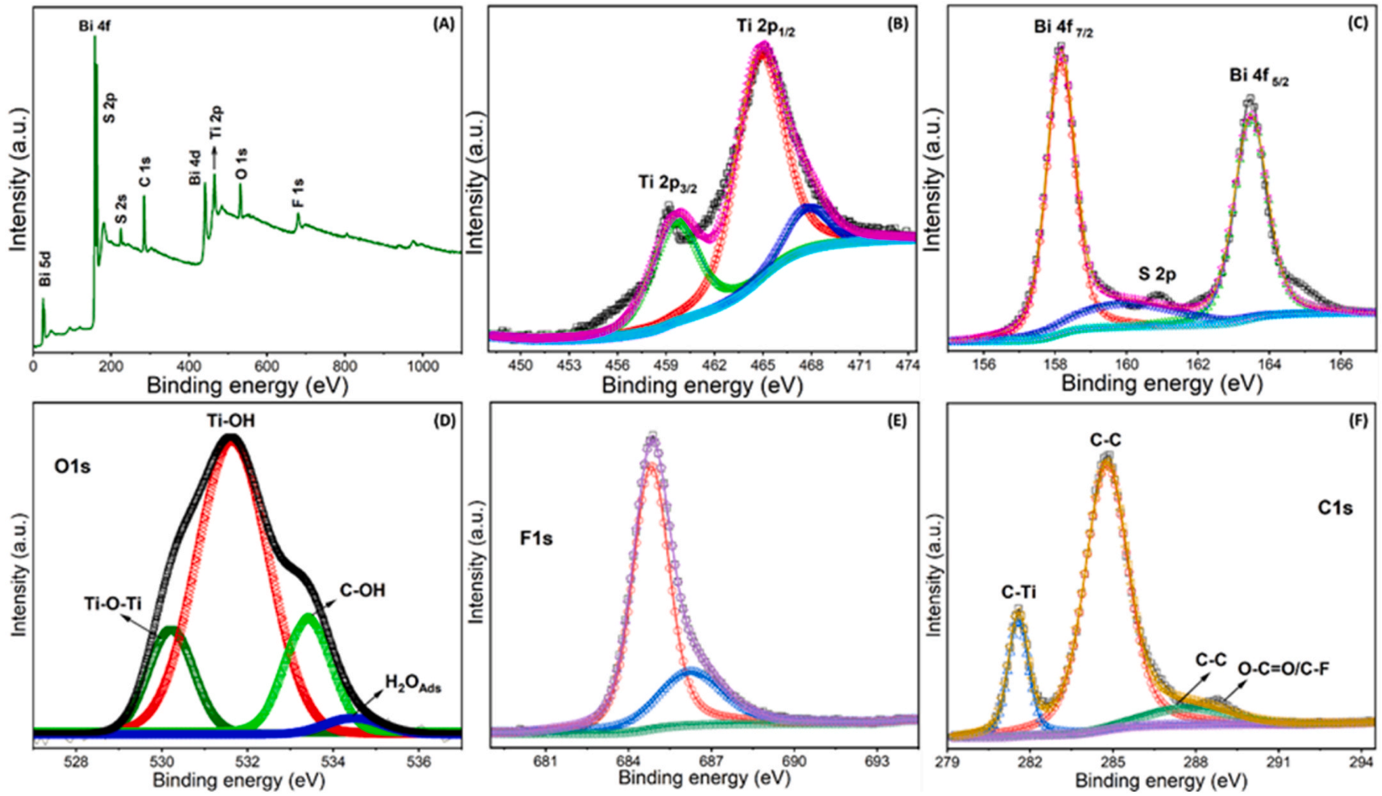

Fig. 3. XPS spectra of **(A)** Bi2S3 -MXene nanocomposite; **(B)** Ti $2p_{1/2}$ peak; **(C)** Bi 4 $f_{7/2}$ **(D)** oxygen 1 s; **(E)** fluorine 1 s; **(F)** carbon 1 s peak.

two peaks: one at 530.0 eV, which represents oxygen atoms bonded to metal atoms (M-O bonds) and another at 531.6 eV, indicating oxygen atoms bonded to oxygen atoms (O-O bonds) (Fig. 3**D**). The XPS spectrum of fluorine 1 s (F 1 s) in the image displays a single peak at 687.6 eV, which is consistent with fluorine **(**Fig. 3**E)** [57]**.** In the C 1 s spectrum of the Bi_2S_3-MXene nanocomposite, there is a peak at 285.0 eV (Fig. 3**F**) [58]. Here, XPS plays a role in providing the information needed to understand the chemical structure of the Bi_2S_3-MXene element being studied. This valuable data reveals a noteworthy relationship between MXene and Bi_2S_3 alone and its nanocomposites, which enhances electron conductivity and facilitates electron transfer. These discoveries align perfectly with the supporting evidence from IR, XRD and XPS analysis.

3.4. *Electrochemical measurements*

First, to analyse the performance of the SPE and modified electrodes (SPE, MXene/SPE, Bi_2S_3/SPE, Bi_2S_3-MXene nanocomposites/SPE), we conducted electrochemical impedance spectroscopy (EIS) and cyclic voltammetry (CV) experiments. Further, to carried out EIS and CV measurements, a PalmSens 4 potentiostat was used. The experiment involved drop casting of 100 µL of solution containing 5 mM potassium ferricyanide/potassium ferrocyanide $[Fe(CN)_6]^{3-/4-}$ dissolved in 0.1 M KCl on top of the strip. Based on the results, we selected Bi_2S_3-MXene nanocomposites dispersion for further experiments. We used 0.05 M acetate buffer with 0.05 M NaCl at pH 4.7 for SWASV to detect Zn(II). The experiments involved detecting Zn (II) concentrations up to 3 µg/mL with the optimised parameters.

3.4.1. *Evaluation of electrocatalytic performance by EIS and CV responses in $[Fe(CN)_6]^{3-/4-}$ solution*

EIS and CV were used as an electrochemical characterization technique for Bi_2S_3-MXene nanocomposites. It provides valuable insights into the redox behavior, electrochemical stability, and charge transfer kinetics of the material. To achieve this, we first modified the SPE electrodes using different nanomaterial dispersions, specifically MXene, Bi_2S_3, and Bi_2S_3-MXene nanocomposites, employing an 8 µL drop-casting technique. To compare their effectiveness, we evaluated SPEs developed using carbon-based ink. For both (EIS & CV), we utilized 5 mM $[Fe(CN)_6]^{3-/4-}$ solution dissolved in 0.1 M KCl. This particular electrolyte was chosen to evaluate the characteristics features of the electrode. Fig. 4**A and B** presents the findings from the EIS and CV experiments.

The EIS plot (Fig. 4**A**) shows that the bare SPE (green curve), exhibits the highest impedance, indicating significant resistance to electron transfer. The MXene/SPE (blue), displays lower impedance compared to the bare electrode, suggesting enhanced electron transfer properties due to the conductive nature of MXene. The Bi_2S_3/SPE (black), also shows reduced impedance compared to the bare electrode, which can be attributed to the catalytic properties of bismuth. The Bi_2S_3-MXene nanocomposite/SPE, (shown in red, on the graph) exhibits the reduced impedance compared to all electrodes, highlighting the synergistic effect of combining MXene and Bi_2S_3. The performance is greatly improved by reducing the resistance to charge transfer and boosting the conductivity of the surface. This enhancement is vital, for applications that need electron transfer procedures.

The CV curves for the bare SPE are used as a reference to compare with modified electrodes: MXene/SPE, Bi_2S_3/SPE, and Bi_2S_3-MXene nanocomposite/SPE (Fig. 4**B**). These comparisons reveal the enhanced electrochemical performance due to modifications with Bi_2S_3, MXene, or their nanocomposite, indicating improved electrochemical behavior over the bare SPE. These enhancements include increased currents, modified redox potentials, improved electrochemical stability, and efficient charge-transfer kinetics. CV experiments provide evidence of two peaks, both in shape and intensity, observed for each modified electrode. These findings align with the reversibility of the redox probes used in the study [59,60].

We compared all the electrodes by measuring the peak heights and the potential difference between anodic peaks. The results showed that

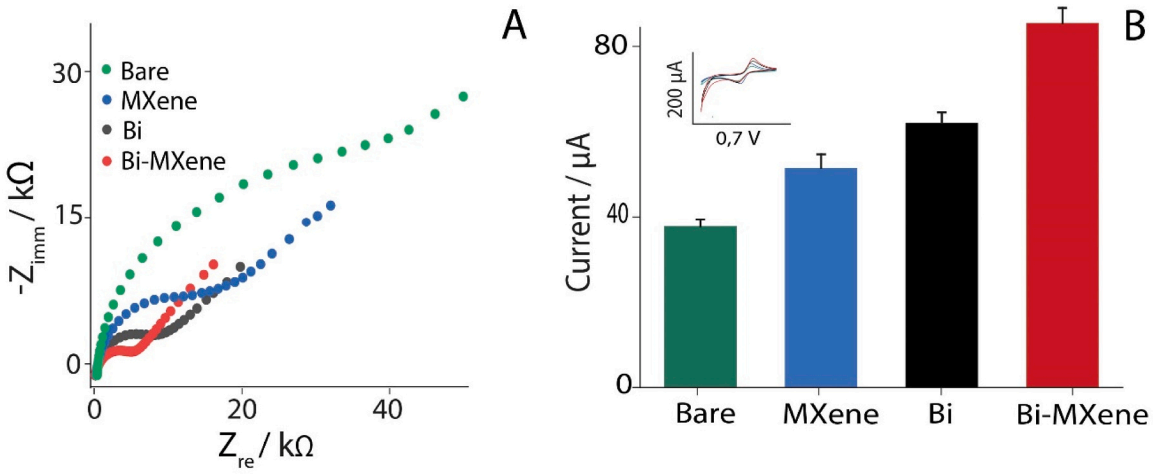

Fig. 4. Electrochemical performance of bare SPEs (green), MXene/SPE (blue), Bi_2S_3 /SPE (black), and Bi_2S_3-MXene nanocomposite/SPE (red) comparison by techniques **(A)** Nyquist plots of the EIS data; Experimental conditions: Frequency range from 0.1 Hz to 100000.0 Hz with 59 points measured; **(B)** Bar graph showing the peak current responses for each electrode configuration **Insert:** CV curves of each electrode. Experimental conditions (for CV): t equilibration=0 s, E begin = −0.8 V; E vertex1 = −0.8 V; E vertex2 = 0.8 V; E step = 0.01 V; scan rate = 0.05 V/s. EIS and CV was measured in a solution containing 5 mM potassium ferricyanide/ferricyanide 5 mM $[Fe(CN)_6]^{3-/4-}$ dissolved in 0.1 M KCl.

each electrode configuration displayed responses in our CV analysis. The bare SPE exhibited a peak current (Ipa) of 38 μA and a peak potential separation (ΔE) of 0.282 V. These values serve as a baseline for comparison with the modified electrodes. The introduction of MXene to the SPE resulted in an increase in the peak current to 52 μA, indicating improved electrochemical activity. Furthermore, there was a decrease, in the separation of peak potentials to 0.245 V, which suggests a shift in the redox potentials. This indicates that the presence of the MXene component has an impact, on the behavior by aiding charge transfer and altering the electronic characteristics of the electrode. Similarly, the electrode that was modified with Bi_2S_3 exhibited enhancements in its functionality. Bi_2S_3/SPE exhibited a peak current of 62 μA with peak potentials measuring 0.265 V. The higher peak current indicates that the electrochemical activity has improved because of Bi_2S_3, which could serve as a material. A notable improvement was seen in the Bi_2S_3-MXene nanocomposite/SPE, with a peak current of 86 μA and a greater separation in peak potential of 0.339 V. The integration of Bi_2S_3 and MXene together, results in improvement of electrochemical behavior with higher peak current, charge transfer due to availability of larger surface area for electron mobility. Hence, on the basis of peak currents and the separation between peak potentials, we choose Bi_2S_3-MXene nanocomposites as a material for detection of Zn (II).

3.5. Optimization of experimental factors for detection of Zn (II)

The optimization of pH and other experimental conditions in SWASV for detecting Zn (II) ions is an important that affect the accuracy, sensitivity, and reproducibility of the technique. This optimization ensures a controlled electrochemical environment, minimizes interference, and maximizes the analytical performance of SWASV, enabling reliable detection of Zn(II).

3.5.1. Optimization of pH

The optimization of pH for Zn(II) detection was carried out at three different pH i.e. 3.7, 4.7, and 5.7 using SWASV technique and current response was measured. The results indicated that the current response increased with increase in pH from 3.7 to 5.7 acetate buffer. The current was observed to be less at pH 3.7 (3.4 μA), it signify that the sensor is less sensitive. Among the other two pH study, stable, and reproducible platform was observed at pH 4.7 (8.6 μA) with less deviation, where as incase of pH 5.7 (10 μA) having more deviation was observed. So based on stability and reproducibility, we selected pH 4.7 in our study as shown in (Fig. 5**A**).

3.5.2. Optimization of deposition time

Selecting the right deposition time is crucial in SWASV since it directly impacts the quantity of Zn (II) deposited on the surface. Increasing the deposition time allows for an accumulation of Zn (II), resulting in a signal response during the subsequent stripping process. We assessed deposition times ranging from 100 s to 400 s and the corresponding currents (μA). Among the tested deposition times, the current values obtained at 300 s (11 μA) indicated a significant increase compared to the shorter deposition times (100 s and 200 s). However, the current value at 400 s (12 μA) did not substantially improve compared to 300 s. Furthermore, the current at 300 s is relatively stable and exhibits less deviation than at 400 s. A stable and consistent current response is desirable as it ensures reliable and reproducible measurements. The lower deviation at 300 s suggests a reduced noise level and better control over the Zn (II) deposition process, as shown in Fig. 5**B**. A deposition period of 300 s was employed for the experiments.

3.5.3. Optimization of deposition potential

When depositing metals electrochemically, it is expected to explore a range of deposition potentials to identify the optimal conditions for the desired outcome. The potential at which the highest current density is achieved typically indicates the most favourable conditions for deposition. Based on the given data, it appears that the Zn (II) deposition potential (-1.5 V) was selected for the study because it demonstrated a higher current (13 μA) and less noise compared to other tested potentials (-1.2 V, −1.3 V, and −1.4 V) and making it the preferred choice for the study as shown in Fig. 5**C.** The selected deposition potentials offered a solution ensuring both the sensitivity of the peak and a controlled background response.

3.5.4. Optimization of square wave frequency

In the optimization study on square wave frequency and current in μA, four frequencies were tested: 25 Hz, 50 Hz, 75 Hz and 100 Hz. At 25 Hz, the current was measured to be 12 μA. As the frequency increased to 50 Hz, the current slightly increased to 12 μA. This indicates a minimal change in current between 25 Hz and 50 Hz. However, when the frequency was further increased to 75 Hz, the current noticeably increased to 14 μA. At 100 Hz, we observed a rise in the current measuring at 16 μA. The frequency of 50 Hz appears to exhibit saturated output, which indicates that the conditions at this frequency are

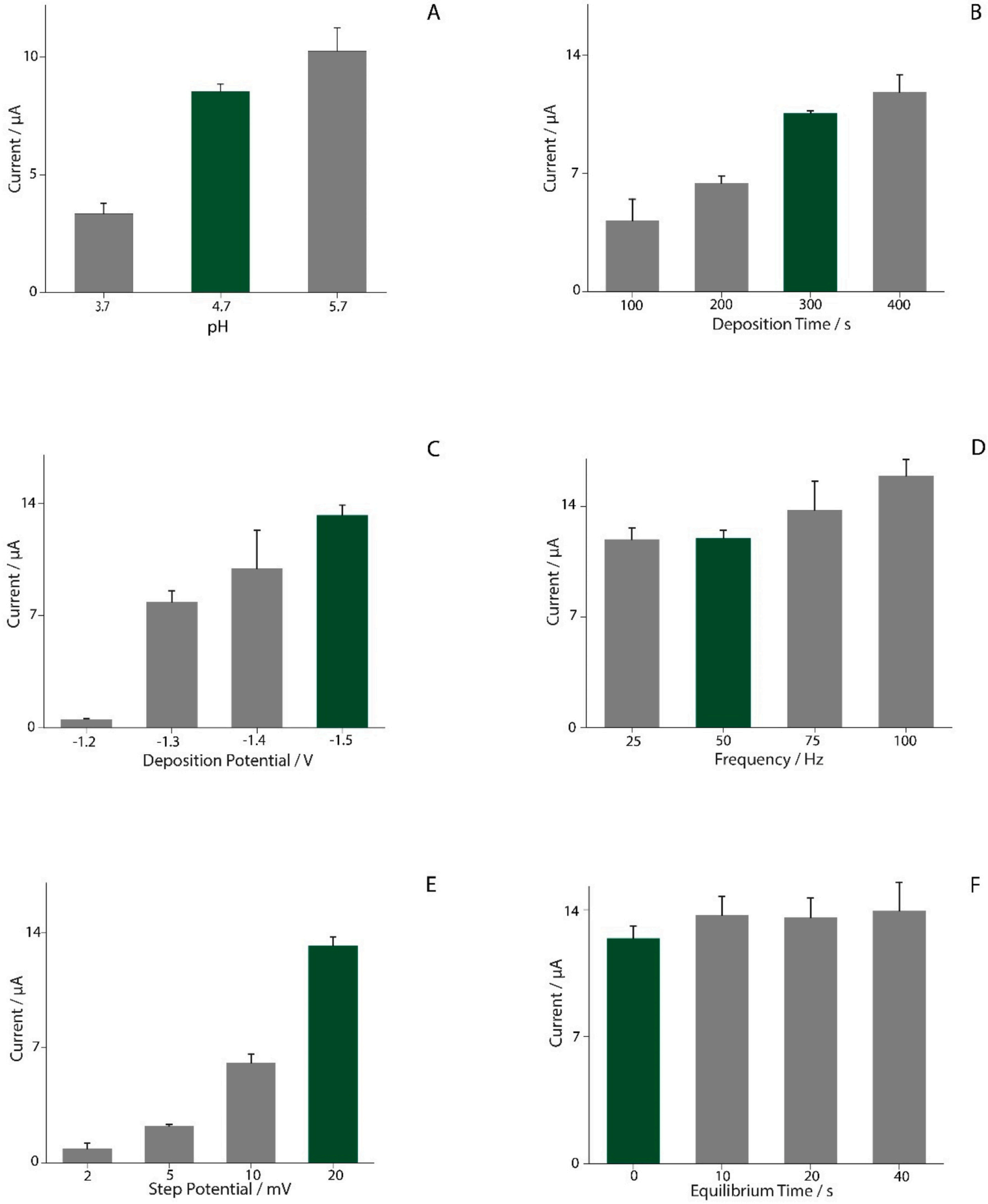

Fig. 5. Optimization of experimental parameters: **(A)** Effect of pH on the detection of Zinc at varying pH levels (3.7, 4.7, and 5.7); **(B)** Optimization of Zn (II) deposition time (100–400 s), Experimental parameters: E dep = −1.5 V, frequency = 50 Hz, E amp = 0.02 V, E step = 0.02 V, t eq = 0 s; **(C)** Optimization of Zn (II) deposition potential (-1.5, −1.4, −1.3 and −1.2 V), Experimental parameters: t dep = 300 s, frequency = 50 Hz, E amp = 0.02 V, E step = 0.02 V, t eq = 0 s; **(D)** Optimization of square wave frequency (25, 50, 75 and 100 Hz), Experimental parameters: E dep = −1.5 V, t dep = 300 s, E amp = 0.02 V, E step = 0.02 V, t eq = 0 s; **(E)** Optimization of square wave step potential (2, 5, 10 and 20 mV), Experimental parameters: E dep = −1.5 V, t dep = 300 s, E amp = 0.02 V, frequency = 50 Hz, t eq = 0 s; **(F)** Optimization of the equilibrium time (0, 10, 20 and 40 s), Experimental parameters: E dep = −1.5 V, t dep = 300 s, frequency = 50 Hz, E amp = 0.02 V, E step = 0.02 V. All the measurements were carried out in triplicate in presence of 1 µg/mL Zn (II) in 0.05 M acetate buffer containing 0.05 M NaCl (pH 4.7).

conducive to the desired process, potentially resulting in enhanced efficiency and reliability, as illustrated in Fig. 5**D**.

3.5.5. Optimization of square wave step potential

In our research on improving the efficiency of square wave step potential and current, we investigated four-step potentials: 2 millivolts (mV), 5 mV, 10 mV and 20 mV. At 2 mV, the measured current was found to be 1 µA. As the step potential was raised to 5 mV, the current rose to 2 µA, indicating an enhancement in flow. Further increasing the step potential to 10 mV resulted in a current of 6 µA, signifying an improvement compared to the steps. However, at 20 mV there was a significant rise in current reaching a value of 13 µA. It's evident that by increasing the step potential, there is an increase in the current. The current values, at 20 mV, showed an improvement as compared to the other tested step potentials, as depicted in Fig. 5**E**.

3.5.6. *Optimization of the equilibrium time*

During the optimization study to determine the time and current for equilibrium, we optimised at four different time points: 0 s, 10 s, 20 s, and 40 s. At 0 s, the current was measured to be 12 μA. As the equilibrium time increased to 10 s, the current slightly increased to 13 μA. However, at 20 s, the current decreased. Finally, at 40 seconds, the current increased slightly to 14 μA. After analyzing the results, we decided to focus on the equilibrium time of 0 s for investigation. The rationale for selecting 0 s was based on the system to achieve equilibrium upon initiation with a more stable current, as shown in Fig. 5**F**.

3.6. *Analytical sensing performances for Zn (II) in standard solutions by SWASV*

SWASV technique was used to improve the sensitivity. Through this study, we observed defined peaks that demonstrate precision in both their shape and place. Such precision is crucial for ensuring concentration measurements. The correlation between the current and concentration is a characteristic of an ideal analytical method. It simplifies the calibration process and further endorses quantification. This relationship guarantees that the current measured is directly proportional to the concentration, making it easier to determine analyte levels without complications. The observed interdependence between the current and concentration is linear up to 3 μg/mL, as depicted in Fig. 6**,** in an acetate buffer at pH 4.7. A relationship between the current (μA) and the concentration of Zn (II) (μg/mL) was established using the equation y= (12.8x - 1.5), resulting in an r^2 value of 0.9825. The limit of detection (LOD) has been determined as 3σB/s, where σB represents the deviation calculated for measurements and s is the slope of the calibration curve. The limit of quantification (LOQ) is calculated as 3.3 times the LOD value. For this analysis, the standard deviation calculated for blank measurements and LOD was 7 ng/mL and LOQ was 22 ng/mL.

The performance of the Bi_2S_3-MXene nanocomposite was found to be better, in terms of both sensitivity and accuracy, compared to the SPE, as well as SPEs modified with MXene and Bi_2S_3. The regression equations, correlation coefficient (r^2), slope and standard error for these materials are presented in Supplementary material.

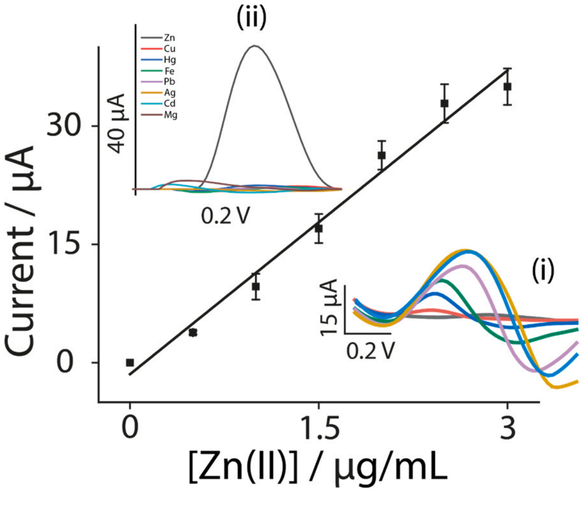

Fig. 6. Calibration curve of peak current value plotted against Zn (II) concentrations up to 3 μg/mL. **Inset (i)** shows the stripping voltammograms performed by Bi_2S_3-MXene nanocomposite/SPEs in presence of Zn (II) concentrations up to 3 μg/mL; Experimental parameters: E dep = −1.5 V, t dep = 300 s, frequency = 50 Hz, E amp = 0.02 V, E step = 0.02 V, t eq = 0 s; Measurements were carried out in 0.05 M acetate buffer containing 0.05 M NaCl (pH 4.7); **Inset (ii)** Stripping voltammograms performed in presence of different heavy metals. Experimental parameters: E dep = −1.5 V, t dep = 300 s, frequency = 50 Hz, E amp = 0.02 V, E step = 0.02 V, t eq = 0 s; Measurements were carried out in triplicate in presence of 1 μg/mL Zn (II) in 0.05 M acetate buffer containing 0.05 M NaCl (pH 4.7).

The regression equations and r^2 values provide evidence that the Bi_2S_3-MXene nanocomposite shows promise as a material for electrochemical sensing applications. It offers improved sensitivity, accuracy and represents a significant advancement in the field of electroanalytical chemistry. Additionally, we compared the properties of Bi_2S_3-MXene/SPE with Zn (II) sensors mentioned in previous studies. For an overview of these properties, please refer to Table 1.

3.7. *Detection of Zn (II) in tap water and seawater*

In our study, we performed a comprehensive validation of our analytical methods for assessing sensitivity, accuracy, precision, and bias (Table 2).

To determine the effectiveness and accuracy of the selected technique, a recovery rate is close to 100 % for both tap water and sea water at 0.5–1.0 μg/mL with % recovery of 99.5–106 %, which is almost close with the true value. Hence, it shows the technique provide good accuracy and approach is reliable. Further, to measure the precision, relative standard deviation (RSD %) was calculated. There was some variability in RSD % for tap water (0.5 μg/mL; RSD =17 %) as compared to 1.0 μg/mL with 7.10 % RSD. Where as in case of sea water shows better precision with 3 % and 1.4 % RSD at 0.5 μg/mL and 1.0 μg/mL, respectively. Systematic error was obtained by Bias (%). In case of tap water at 0.5 μg/mL has a bias of 6 %, while at 1.0 μg/mL, the bias is −0.5 %. Whereas incase of sea water bias values were 0.5 % and 5.7 % for 0.5 μg/mL and 1.0 μg/mL. The comparative bias % results among tap and sea water shows acceptable LOD and LOQ are critical parameters in determining the sensitivity of the method. The LOD for tap water was found to be 19 ng/mL and LOQ (63 ng/mL), subsequently for sea water LOD was found to be 25 ng/mL and LOQ (84 ng/mL).

In summary, the outcome of results of Table 2 demonstrates that the analytical methods are reliable with good recovery and precision for both tap water and sea water particularly at the higher concentration. The sensitivity of the developed sensor was observed good for both and indicated by the LOD and LOQ.

3.8. *Selectivity study*

The graph presented in Fig. 6 is focus on the detection of Zn (II) and evaluating if any interference caused by the presence of other metal ions such as Cu, Hg, Fe, Pb, Ag, Cd, and Mg. To this, separate solution of 1 μg/mL of each metal (Zn, Cu, Hg, Fe, Pb, Ag, Cd, and Mg) was prepared and further the experiment was carried out by using Bi_2S_3-MXene/SPE. Under optimised conditions, response such as changes in current or voltage, was observed for each metal. From the graph, prominent strong and clear signal/ or peak for Zn (II) was observed, while there is no response for the other metal. The outcome of the result suggest that the material is highly selective and sensitive to Zn (II) detection. The material and method is reliable, making the method suitable for applications where selective detection of Zn is required.

4. Conclusion

In this study, a novel electrochemical sensing platform is developed by using Bi_2S_3-MXene nanocomposite. The shape, composition and electrical characteristics of the prepared composites and their modified electrodes were investigated using SEM, XRD, XPS, and various electrochemical techniques. Subsequently, the detection of Zn (II) was performed using the SWASV electrochemical technique under optimal parameters. As shown in the experimental results, the technique is highly sensitive and selective for Zn (II) with LOD of 7 ng/mL and LOQ was 22 ng/mL in the linearity range up to 3 μg/mL. The applicability of the system was further evaluated using real environmental samples,

Table 1
Performance comparison of various reported Zn (II) sensors.

Electrode material	Technique	Detection limit (ng/mL)	Linearity range (µg/mL)	Performance	Cost Implications (Based on procedure and materials)	References
MWCNTs/CS/PB/AuE	differential pulse voltammetry (DPV)	260	0.2–7.0	Moderate to high sensitivity and selectivity	Moderate to high costs due to operational costs	[61]
Calix/MPA/Au	DPV	1500	2.85–6.65	Low sensitivity and selectivity	High material and operational costs	[62]
Bi_2S_3	SWASV	25	0.08–2	Medium sensitivity	Medium cost	[63]
Carbon nanotube immobilized cellulose yar	DPV	<1000	0.1–500	Low sensitivity and selectivity	High operational costs	[64]
Ti_3C_2(HF)/Fe_3O_4/g-C_3N_4	DPASV	0.26	0.0005–0.005	High sensitivity and selectivity	High material and operational costs	[23]
HDPBA—MWCNTs/CPE	SWASV	2.48	0.02–10	High sensitivity and selectivity	High material and operational costs	[65]
Bi_2S_3 film-modified Electrode	DPASV	16.7	0.0765–1.683	Medium sensitivity and high selectivity	Economical material and operational cost	[66]
Bi_2S_3-MXene nanocomposite	SWASV	7	Up to 3.0	High sensitivity and selectivity	Economical material costs; scalable screen printing; simple procedure	This work

Table 2
Comparative analytical methods for assessing sensitivity, accuracy, precision, and bias in tap water and sea water sample.

Sample type	Concentration (µg/mL	% Recovery (Found concentration/Original concentration) ∗ 100	Relative standard deviation (RSD %)= (Standard deviation/Mean) ∗ 100	Bias (%)= (Measured value − True value/True value) ∗ 100	LOD (ng/ mL)	LOQ (ng/ mL)
Tap water	0.5	106	17.5	6	19	63
Tap water	1.0	99.5	7.1	-0.5		
Sea water	0.5	100.5	3.2	0.5	25	84
Sea water	1.0	105.7	1.4	5.7		

Stefano Cinti

specifically tap water and sea water. The results of the analysis of these real samples demonstrated the practical applicability of the sensor. Compared to other detection methods, the novel electrochemical detection assay offers a low-cost, user-friendly platform for detecting Zn (II). This approach is anticipated to replace complex and labor-intensive analyses, showing significant potential for future advancements.

CRediT authorship contribution statement

Wanda Cimmino: Writing – review & editing, Formal analysis. **Arshid Numan:** Writing – original draft, Formal analysis. **Sima Singh:** Writing – original draft, Investigation, Funding acquisition. **Ada Raucci:** Writing – review & editing, Formal analysis. **Mohammad Khalid:** Writing – review & editing, Formal analysis. **Stefano Cinti:** Writing – review & editing, Validation, Supervision, Funding acquisition, Conceptualization.

Declaration of Competing Interest

The authors declare the following financial interests/personal relationships which may be considered as potential competing interests: Stefano Cinti reports financial support was provided by The authors acknowledge the Department of Excellence 2023–2027 grant from the MUR. If there are other authors, they declare that they have no known competing financial interests or personal relationships that could have appeared to influence the work reported in this paper.

Data availability

Data will be made available on request.

Acknowledgements

The authors acknowledge the Department of Excellence 2023–2027 grant from the MUR. MacDermid Alpha - Film & Smart Surface Solutions is aknowledged for providing the polyester sheets Autostat HT5.

Appendix A. Supporting information

Supplementary data associated with this article can be found in the online version at doi:10.1016/j.snb.2024.136219.

References

[1] A. Hakimifar, A. Morsali, Urea-based metal-organic frameworks as high and fast adsorbent for Hg 2+ and Pb 2+ removal from water, Inorg. Chem. 58 (2019) 180–187, https://doi.org/10.1021/acs.inorgchem.8b02133.

[2] B. Deng, R.A. Carter, Y. Cheng, Y. Liu, L. Eddy, K.M. Wyss, M.G. Ucak-Astarlioglu, D.X. Luong, X. Gao, K. JeBailey, C. Kittrell, S. Xu, D. Jana, M.A. Torres, J. Braam, J. M. Tour, High-temperature electrothermal remediation of multi-pollutants in soil, Nat. Commun. 14 (2023) 6371, https://doi.org/10.1038/s41467-023-41898-z.

[3] Z. Rahman, V.P. Singh, The relative impact of toxic heavy metals (THMs) (arsenic (As), cadmium (Cd), chromium (Cr)(VI), mercury (Hg), and lead (Pb)) on the total environment: an overview, Environ. Monit. Assess. 191 (2019) 1–21, https://doi.org/10.1007/s10661-019-7528-7.

[4] H. Liu, M. Baghayeri, A. Amiri, F. Karimabadi, M. Nodehi, M. Fayazi, B. Maleki, E. N. Zare, A. Kaffash, A strategy for As(III) determination based on ultrafine gold nanoparticles decorated on magnetic graphene oxide, Environ. Res. 231 (2023) 116177, https://doi.org/10.1016/j.envres.2023.116177.

[5] M. Fayazi, M.A. Taher, D. Afzali, A. Mostafavi, Fe3O4 and MnO2 assembled on halloysite nanotubes: A highly efficient solid-phase extractant for electrochemical detection of mercury(II) ions, Sens. Actuators, B Chem. 228 (2016) 1–9, https://doi.org/10.1016/j.snb.2015.12.107.

[6] V. Herrera, Reconciling global aspirations and local realities: Challenges facing the Sustainable Development Goals for water and sanitation, World Dev. 118 (2019) 106–117, https://doi.org/10.1016/j.worlddev.2019.02.009.

[7] Heavy metal emissions in Europe, (2023). 〈https://www.eea.europa.eu/en/analysis/indicators/heavy-metal-emissions-in-europe?activeAccordion=ecdb3bcf-bbe9-4978-b5cf-0b136399d9f8〉.

[8] A. Zhuravlova, A.G. Ricciardulli, D. Pakulski, A. Gorczyński, A. Kelly, J. N. Coleman, A. Ciesielski, P. Samorì, High selectivity and sensitivity in chemiresistive sensing of Co(II) ions with liquid-phase exfoliated functionalized MoS2: a supramolecular approach, Small (2023) 2208100, https://doi.org/10.1002/smll.202208100.

[9] K. Hanaoka, K. Kikuchi, H. Kojima, Y. Urano, T. Nagano, Selective detection of zinc ions with novel luminescent lanthanide probes, Angew. Chem. - Int Ed. 42 (2003) 2996–2999, https://doi.org/10.1002/anie.200351122.

[10] L.A. Escudero, L.D. Martinez, J.A. Salonia, J.A. Gasquez, Determination of Zn(II) in natural waters by ICP-OES with on-line preconcentration using a simple solid phase extraction system, Microchem J. 95 (2010) 164–168, https://doi.org/10.1016/j.microc.2009.11.003.

[11] S. Hajialigol, M.A. Taher, A. Malekpour, Determination of trace amounts of zinc by flame atomic absorption spectrometry after preconcentration with modified clinoptilolite zeolite, J. AOAC Int 91 (2008) 1446–1452, https://doi.org/10.1093/jaoac/91.6.1446.

[12] L.Y. Shen, X.L. Chen, X.J. Yang, H. Xu, Y.L. Huang, X. Zhang, C. Redshaw, Q. L. Zhang, A highly selective turn-on fluorescent probe for the detection of zinc, Molecules 26 (2021) 3825, https://doi.org/10.3390/molecules26133825.

[13] S. Enbanathan, S. Munusamy, D. Jothi, S. Manojkumar, S. Manickam, S.K. Iyer, Zinc ion detection using a benzothiazole-based highly selective fluorescence “turn-on” chemosensor and its real-time application, RSC Adv. 12 (2022) 27839–27845, https://doi.org/10.1039/d2ra04874d.

[14] L.C. Costello, R.B. Franklin, Energy Dispersive X-Ray Fluorescence Zn/Fe ratiometric determination of zinc levels in expressed prostatic fluid: a direct, non-invasive and highly accurate screening for prostate cancer, Acta Sci. Cancer Biol. 2 (2018) 33.

[15] S. Cinti, D. Moscone, F. Arduini, Preparation of paper-based devices for reagentless electrochemical (bio)sensor strips, Nat. Protoc. 14 (2019) 2437–2451, https://doi.org/10.1038/s41596-019-0186-y.

[16] S. Cinti, Novel paper-based electroanalytical tools for food surveillance, Anal. Bioanal. Chem. 411 (2019) 4303–4311, https://doi.org/10.1007/s00216-019-01640-5.

[17] Z. Xue, W. Zhao, T. Mu, Electrochemistry, Deep Eutectic Solvents Synth. Prop. Appl. (2019) 8804–8810, https://doi.org/10.1002/9783527818488.ch17.

[18] E.T.S.G. da Silva, D.E.P. Souto, J.T.C. Barragan, J. de, F. Giarola, A.C.M. de Moraes, L.T. Kubota, Electrochemical biosensors in point-of-care devices: recent advances and future trends, ChemElectroChem 4 (2017) 778–794, https://doi.org/10.1002/celc.201600758.

[19] J. Zheng, M.A. Rahim, J. Tang, F.M. Allioux, K. Kalantar-Zadeh, Post-transition metal electrodes for sensing heavy metal ions by stripping voltammetry, Adv. Mater. Technol. 7 (2022) 2100760, https://doi.org/10.1002/admt.202100760.

[20] H. Yin, H. He, T. Li, M. Hu, W. Huang, Z. Wang, X. Yang, W. Yao, F. Xiao, Y. Wu, Y. Sun, Ultra-sensitive detection of multiplexed heavy metal ions by MOF-derived carbon film encapsulating BiCu alloy nanoparticles in potable electrochemical sensing system, Anal. Chim. Acta 1239 (2023) 340730, https://doi.org/10.1016/j.aca.2022.340730.

[21] L.M. Plum, L. Rink, H. Hajo, The essential toxin: Impact of zinc on human health, Int J. Environ. Res Public Health 7 (2010) 1342–1365, https://doi.org/10.3390/ijerph7041342.

[22] J. Qin, W. Li, K. Cai, D. Wang, C. Peng, L. Luo, S. Song, Y. Mei, Y. Wang, Simultaneous electrochemical detection of zinc and copper in fruit juice using Hg/CMWCNTs@ZIF-8 modified glassy carbon electrode, Microporous Mesoporous Mater. 360 (2023) 112721, https://doi.org/10.1016/j.micromeso.2023.112721.

[23] M. Akhtar, M. Sohail, M. Farooq Warsi, M.M. Ibrahim, M.A. Amin, M. Shahid, Fe3O4 nanochips loaded MXenes/g-C3N4 nanocomposite for ultrasensitive electrochemical detection of zinc (II), cadmium (II), lead (II), copper (II) and mercury (II) metal ions, FlatChem 41 (2023) 100537, https://doi.org/10.1016/j.flatc.2023.100537.

[24] T. Kokulnathan, R. Vishnuraj, T.J. Wang, E.A. Kumar, B. Pullithadathil, Heterostructured bismuth oxide/hexagonal-boron nitride nanocomposite: a disposable electrochemical sensor for detection of flutamide, Ecotoxicol. Environ. Saf. 207 (2021) 111276, https://doi.org/10.1016/j.ecoenv.2020.111276.

[25] K. Takemura, T. Motomura, W. Iwasaki, N. Morita, Fabrication of highly active nanoneedle gold electrode using rose petals for electrochemical detection of Arsenic(III), ACS Appl. Nano Mater. 6 (2023) 15879–15886, https://doi.org/10.1021/acsanm.3c02781.

[26] M. Branca, K. Corp, D. Ciuculescu-Pradines, Y. Coppel, P. Lecante, C. Amiens, Insights into the chemistry of bismuth nanoparticles, New J. Chem. 41 (2017) 5960–5966, https://doi.org/10.1039/c7nj01308f.

[27] Y. Zhang, Y. Qin, L. Jiao, H. Wang, Z. Wu, X. Wei, Y. Wu, N. Wu, L. Hu, H. Zhong, W. Gu, C. Zhu, Atomically thin bismuthene nanosheets for sensitive electrochemical determination of heavy metal ions, Anal. Chim. Acta 1235 (2022) 340510, https://doi.org/10.1016/j.aca.2022.340510.

[28] J. Ganesamurthi, R. Shanmugam, S.M. Chen, P. Veerakumar, Bismuth sulfide/zinc-doped graphitic carbon nitride nanocomposite for electrochemical detection of hazardous nitric oxide, J. Electro Chem. 910 (2022) 116174, https://doi.org/10.1016/j.jelechem.2022.116174.

[29] M. Naguib, M. Kurtoglu, V. Presser, J. Lu, J. Niu, M. Heon, L. Hultman, Y. Gogotsi, M.W. Barsoum, Two-dimensional nanocrystals: two-dimensional nanocrystals produced by exfoliation of Ti3AlC2 (Adv. Mater. 37/2011), Adv. Mater. 23 (2011), https://doi.org/10.1002/adma.201190147.

[30] A. Sinha, Dhanjai, H. Zhao, Y. Huang, X. Lu, J. Chen, R. Jain, MXene: An emerging material for sensing and biosensing, TrAC - Trends Anal. Chem. 105 (2018) 424–435, https://doi.org/10.1016/j.trac.2018.05.021.

[31] M.Q. Zhao, C.E. Ren, Z. Ling, M.R. Lukatskaya, C. Zhang, K.L. Van Aken, M. W. Barsoum, Y. Gogotsi, Flexible MXene/carbon nanotube composite paper with high volumetric capacitance, Adv. Mater. 27 (2015) 339–345, https://doi.org/10.1002/adma.201404140.

[32] X. Wu, P. Ma, Y. Sun, F. Du, D. Song, G. Xu, Application of MXene in Electrochemical Sensors: A Review, Electroanalysis 33 (2021) 1827–1851, https://doi.org/10.1002/elan.202100192.

[33] G. Wang, F. Wang, P. Deng, J. Li, C. Wang, Y. Hua, Y. Shen, X. Tian, Electronic modulation of two-dimensional bismuth-based nanosheets for electrocatalytic CO2 reduction to formate: A review, Mater. Rep. Energy 3 (2023) 100181, https://doi.org/10.1016/j.matre.2023.100181.

[34] F. Ezzah, A. Latif, A. Numan, N. Mujawar, M. Khalid, E. Chan, N. Abdul, R. Walvekar, Evolution of MXene and its 2D heterostructure in electrochemical sensor applications, Coord. Chem. Rev. 471 (2022) 214755, https://doi.org/10.1016/j.ccr.2022.214755.

[35] M.N. Mustafa, M.A.A. Mohd Abdah, A. Numan, Y. Sulaiman, R. Walvekar, M. Khalid, Development of high-performance MXene/nickel cobalt phosphate nanocomposite for electrochromic energy storage system using response surface methodology, J. Energy Storage 68 (2023) 107880, https://doi.org/10.1016/j.est.2023.107880.

[36] Z. Othman, H.R. Mackey, K.A. Mahmoud, A critical overview of MXenes adsorption behavior toward heavy metals, Chemosphere 295 (2022) 133849, https://doi.org/10.1016/j.chemosphere.2022.133849.

[37] Y. Zhang, W. Bin Lu, J.P. Zhou, D.Q. Sun, H.M. Li, The multiple synthesis of layered V2CTx-MXene composites with enhanced electrochemical properties, J. Alloy. Compd. 929 (2022) 167276, https://doi.org/10.1016/j.jallcom.2022.167276.

[38] W. Seanghirun, K. Samoson, S. Cotchim, S. Kongkaew, W. Limbut, Green electrochemical sensor for Zn(II) ions detection in human seminal fluid, Microchem J. 157 (2020) 104958, https://doi.org/10.1016/j.microc.2020.104958.

[39] S. Singh, A. Numan, M. Khalid, I. Bello, E. Panza, S. Cinti, Facile and Affordable Design of MXene-Co3O4-based nanocomposites for detection of hydrogen peroxide in cancer cells: toward portable tool for cancer management, Small 19 (2023) 2208209, https://doi.org/10.1002/smll.202208209.

[40] S.C. Endres, L.C. Ciacchi, L. Mädler, A review of contact force models between nanoparticles in agglomerates, aggregates, and films, J. Aerosol Sci. 153 (2021) 105719, https://doi.org/10.1016/j.jaerosci.2020.105719.

[41] A. Boudet, O. Henrotte, N. Limani, F. El Orf, F. Oswald, B. Jousselme, R. Cornut, Unraveling the link between catalytic activity and agglomeration state with scanning electrochemical microscopy and atomic force microscopy, Anal. Chem. 94 (2022) 1697–1704, https://doi.org/10.1021/acs.analchem.1c04256.

[42] F. Maillard, S. Schreier, M. Hanzlik, E.R. Savinova, S. Weinkauf, U. Stimming, Influence of particle agglomeration on the catalytic activity of carbon-supported Pt nanoparticles in CO monolayer oxidation, Phys. Chem. Chem. Phys. (2005) 385–393, https://doi.org/10.1039/b411377b.

[43] A. Bhat, S. Anwer, K.S. Bhat, M.I.H. Mohideen, K. Liao, A. Qurashi, Prospects challenges and stability of 2D MXenes for clean energy conversion and storage applications, Npj 2D Mater. Appl. 5 (2021) 61, https://doi.org/10.1038/s41699-021-00239-8.

[44] T. Su, X. Ma, J. Tong, H. Ji, Z. Qin, Z. Wu, Surface engineering of MXenes for energy and environmental applications, J. Mater. Chem. A 10 (2022) 10265–10296, https://doi.org/10.1039/d2ta01140a.

[45] M.A. Iqbal, A. Tariq, A. Zaheer, S. Gul, S.I. Ali, M.Z. Iqbal, D. Akinwande, S. Rizwan, Ti3C2-MXene/bismuth ferrite nanohybrids for efficient degradation of organic dyes and colorless pollutants, ACS Omega 4 (2019) 0530–0539, https://doi.org/10.1021/acsomega.9b02359.

[46] S. Palei, G. Murali, C.H. Kim, I. In, S.Y. Lee, S.J. Park, A review on interface engineering of MXenes for perovskite solar cells, Nano-Micro Lett. 15 (2023) 1–39, https://doi.org/10.1007/s40820-023-01083-9.

[47] Y. Gogotsi, B. Anasori, The Rise of MXenes, ACS Nano 13 (2019) 8491–8494, https://doi.org/10.1021/acsnano.9b06394.

[48] S. Biswas, P.S. Alegaonkar, MXene: evolutions in chemical synthesis and recent advances in applications, Surfaces 5 (2022) 1–34, https://doi.org/10.3390/surfaces5010001.

[49] J. Lu, Q.F. Han, X.J. Yang, L. De Lu, X. Wang, Study on the preparation and spectral characteristics of Bi2S3 nanoribbons, Spectrosc. Spect. Anal. 29 (2009) 48–51, https://doi.org/10.3964/j.issn.1000-0593(2009)01-0048-04.

[50] Y. Li, X. Zhou, J. Wang, Q. Deng, M. Li, S. Du, Y.-H. Han, J. Lee, Q. Huang, Facile preparation of in situ coated $Ti_3C_2T_x/Ni_{0.5}Zn_{0.5}Fe_2O_4$ composites and their electromagnetic performance, RSC Adv. 7 (2017) 24698–24708, https://doi.org/10.1039/C7RA03402D.

[51] J.E. Heckler, G.R. Neher, F. Mehmood, D.B. Lioi, R. Pachter, R. Vaia, W.J. Kennedy, D. Nepal, Surface functionalization of Ti3C2T xMXene nanosheets with catechols: implication for colloidal processing, Langmuir 37 (2021) 5447–5456, https://doi.org/10.1021/acs.langmuir.0c03078.

[52] C. Sambathkumar, V. Manirathinam, A. Manikandan, M. Krishna Kumar, S. Sudhahar, P. Devendran, Solvothermal synthesis of Bi2S3 nanoparticles for active photocatalytic and energy storage device applications, J. Mater. Sci. Mater. Electron 32 (2021) 20827–20843, https://doi.org/10.1007/s10854-021-06596-w.

[53] P.K. Panigrahi, A. Pathak, The Growth of bismuth sulfide nanorods from spherical-shaped amorphous precursor particles under hydrothermal condition, J. Nanopart. 2013 (2013) 1–12, https://doi.org/10.1155/2013/367812.

[54] S.S. Sangu, N.M. Illias, C.C. Ong, S.C.B. Gopinath, M.S.M. Saheed, MXene-based aptasensor: characterization and high-performance voltammetry detection of deoxynivalenol, Bionanoscience 11 (2021), https://doi.org/10.1007/s12668-021-00847-0.

[55] D.P. Sahu, S.N. Jammalamadaka, Detection of bovine serum albumin using hybrid TiO2 + graphene oxide based Bio – resistive random access memory device, Sci. Rep. 9 (2019) 16141, https://doi.org/10.1038/s41598-019-52522-w.

[56] S. Singh, R.K. Sahoo, N.M. Shinde, J.M. Yun, R.S. Mane, W. Chung, K.H. Kim, Asymmetric faradaic assembly of Bi2O3 and MnO2 for a high-performance hybrid electrochemical energy storage device, RSC Adv. 9 (2019) 32154–32164, https://doi.org/10.1039/c9ra06331e.

[57] M. Boča, P. Barborík, M. Mičušík, M. Omastová, X-ray photoelectron spectroscopy as detection tool for coordinated or uncoordinated fluorine atoms demonstrated on fluoride systems NaF, K 2TaF 7, K 3TaF 8, K 2ZrF 6, Na 7Zr 6F 31 and K 3ZrF 7, Solid State Sci. 14 (2012) 828–832, https://doi.org/10.1016/j.solidstatesciences.2012.04.018.

[58] T. Kokulnathan, S.M. Chen, Robust and selective electrochemical detection of antibiotic residues: The case of integrated lutetium vanadate/graphene sheets architectures, J. Hazard Mater. 384 (2020) 121304, https://doi.org/10.1016/j.jhazmat.2019.121304.

[59] S. Cinti, D. Talarico, G. Palleschi, D. Moscone, F. Arduini, Novel reagentless paper-based screen-printed electrochemical sensor to detect phosphate, Anal. Chim. Acta 919 (2016) 78–84, https://doi.org/10.1016/j.aca.2016.03.011.

[60] C.E. Banks, T.J. Davies, G.G. Wildgoose, R.G. Compton, Electrocatalysis at graphite and carbon nanotube modified electrodes: Edge-plane sites and tube ends are the reactive sites, Chem. Commun. 7 (2005) 829–841, https://doi.org/10.1039/b413177k.

[61] G. Ringgit, S. Siddiquee, S. Saallah, M.T. Mohamad Lal, A sensitive and rapid determination of zinc ion (Zn2+) using electrochemical sensor based on f-MWCNTs/CS/PB/AuE in drinking water, Sci. Rep. 12 (2022) 18582, https://doi.org/10.1038/s41598-022-21926-6.

[62] S.F.N.Abdul Aziz, S.A.A. Ahmad, Electrochemical detection of nickel(II) and zinc (II) ions by a dicarboxyl-Calix[4]arenebased sensor (Calix/MPA/Au) through differential pulse voltammetry analysis, Aqua Water Infrastruct., Ecosyst. Soc. 72 (2023) 160–172, https://doi.org/10.2166/aqua.2023.179.

[63] S. Cinti, B. De Lellis, D. Moscone, F. Arduini, Sustainable monitoring of Zn(II) in biological fluids using office paper, Sens. Actuators, B Chem. 253 (2017) 1199–1206, https://doi.org/10.1016/j.snb.2017.07.161.

[64] S. Mondal, C. Subramaniam, Point-of-Care, Cable-Type Electrochemical Zn2+ Sensor with Ultrahigh Sensitivity and Wide Detection Range for Soil and Sweat Analysis, ACS Sustain Chem. Eng. 7 (2019) 14569–14579, https://doi.org/10.1021/acssuschemeng.9b02173.

[65] E. Tesfaye, B.S. Chandravanshi, N. Negash, M. Tessema, Electrochemical determination of zinc(II) using N1-hydroxy-N1,N2-diphenylbenzamidine and multi-walled carbon nanotubes modified carbon paste electrode, Heliyon 9 (2023) e17346, https://doi.org/10.1016/j.heliyon.2023.e17346.

[66] N.M. Thanh, N. Van Hop, N.D. Luyen, N.H. Phong, T.T.T. Toan, H.D. Mai, Simultaneous Determination of Zn(II), Cd(II), Pb(II), and Cu(II) Using Differential Pulse Anodic Stripping Voltammetry at a Bismuth Film-Modified Electrode, Adv. Mater. Sci. Eng. 2019 (2019) 1–11, https://doi.org/10.1155/2019/1826148.

Sima Singh, currently a Postdoctoral Fellow at Fondazione Umberto Veronesi, is working on enhancing electrochemical systems with nanotechnology for improved detection of bioanalytes and heavy metals. This integration promises to significantly improve the accuracy and efficiency of detecting, monitoring, and analyzing various biochemical substances, which has profound implications for healthcare, environmental monitoring, and beyond. Her innovative research has earned her an MSCA fellowship starting in 2024.

Ada Raucci is currently pursuing her PhD in the Department of Pharmacy at the University of Naples Federico II. Her research focuses on the development of portable electrochemical devices designed for user-friendly applications in both clinical and environmental settings. Additionally, she is a visiting PhD fellow at the University of California, USA.

Wanda Cimmino is currently pursuing her PhD in the Department of Pharmacy at the University of Naples Federico II, where she is deeply involved in cutting-edge research that lies at the intersection of analytical chemistry. Her work is primarily centered on the development and refinement of electrochemical sensors and biosensors. These devices are crucial for detecting and quantifying biological markers and chemical compounds with high sensitivity and specificity.

Numan Arshid is an Associate Professor at the Sunway Centre for Electrochemical Energy and Sustainable Technology (SCEEST), Sunway University, primarily focuses his research on the synthesis and characterization of carbonaceous materials. His work is dedicated to their applications in energy storage devices, as well as electrochemical sensors for bioanalytes and water pollutants.

Professor Mohammad Khalid has more than 10 years of research and teaching experience. He has supervised 11 PhD, eight MSc and one MPhil students, and 13 of these students (four PhD, eight MSc and one MPhil) have graduated. His research specializes in nanomaterial synthesis, heat transfer fluids, phase change materials, and energy harvesting, particularly solar energy harvesting with deep eutectic salts and carbon nanoparticle nanolubricants to enhance engine performance. He has authored over 100 international journal papers and conference proceedings, holds five patents, and has contributed to seven book chapters.

Stefano Cinti is an Associate Professor at the Department of Pharmacy, University of Naples “Federico II”. He obtained a Ph.D. in Chemical Sciences in 2016 in the group headed by Prof. Giuseppe Palleschi at the University of Rome “Tor Vergata”. He leads the uninanobiosensors Lab (uninanobiosensors.com) at University of Naples “Federico II”, and his research interests include the development of electrochemical sensors, portable diagnostics, paper-based devices and nanomaterials. During his research activity, he had the opportunity to spend a period abroad in Finland, U.K., U.S., Germany, and Spain. He has published more than 90 papers in peer-reviewed journals, with an H-index of 35 and ca.5000 citations. Among all the prizes and certificates, in 2018 he was named Best Young Researcher in Bio-Analytical Chemistry, in 2019 he was named Best Young Researcher in Analytical Chemistry (both by the Italian Chemical Society), in 2022 he was awarded with the early career award from International Society of Electrochemistry in Analytical Electrochemistry, in 2022 he was awarded with Biosensors 2022 Young Investigator Award, and in 2021 and 2022 he has been recognized as the World’s Top 2 % Scientists, in 2023 he was included in the Rising Stars by ACS Measurement Science Au. He is the coordinator of the Chemical Cultural Diffusion group of Italian Chemical Society. He is the Chair of AMYC-BIOMED, a multidisciplinary conference for young chemists in the biomedical sciences. He is very active in communicating science to nonspecialized audiences through TV shows, radio, and magazine.